Ultrafast photodissociation dynamics of 1,4-diiodobenzene

This manuscript was accepted by J. Chem. Phys. Click here to see the version of record.

Ultrafast Photodissociation Dynamics of 1,4-diiodobenzene

Brian Stankus[1], Nikola Zotev[2], David M. Rogers[2], Yan Gao[1], Asami Odate[1], Adam Kirrander[2], Peter M. Weber[*1]
[1] *Department of Chemistry, Brown University, Providence, RI 02912, USA*
[2] *EaStCHEM, School of Chemistry, University of Edinburgh, David Brewster Road, Edinburgh EH9 3FJ, UK*

ABSTRACT

The photodissociation dynamics of 1,4-diiodobenzene is investigated using ultrafast time-resolved photoelectron spectroscopy. Following excitation by laser pulses at 271 nm, the excited-state dynamics is probed by resonance-enhanced multiphoton ionization with 405 nm probe pulses. A progression of Rydberg states, which come into resonance sequentially, provide a fingerprint of the dissociation dynamics of the molecule. The initial excitation decays with a lifetime of 33 ± 4 fs, in good agreement with previous studies. The spectrum is interpreted by reference to *ab-initio* calculations at the CASPT2(18,14) level including spin-orbit coupling. We propose that both the $5B_1$ and $6B_1$ states are excited initially, and based on the calculations we identify diabatic spin-orbit coupled states corresponding to the main dissociation pathways.

INTRODUCTION

The addition of substituent atoms and groups to the archetypal aromatic benzene molecule has interesting and profound effects on its chemistry and photophysics. This ranges from the function of aromatic amino acid side chains involved in π stacking and hydrogen-bonding interactions in biological environments, to fundamental spectroscopic events in the gas phase. The addition of a halogen atom to a benzene ring in particular introduces additional electronically excited states, leading to (π,σ*), (n,π*) and (n,σ*) transitions in the UV-Vis region of the spectrum of aryl halides. For the heavier halogens, spin-orbit coupling becomes a key factor in determining the electronic structure, and thus dynamics, in species such as iodobenzene and diiodobenzene (DIB).

As a consequence of the dense manifold of electronic states arising from the perturbations on the aromatic π system due to the substituent, the photodissociation of aryl halides exhibits a rich variety of phenomena. Early photofragment translational energy distribution studies by Bersohn, *et. al.*[1–3] identified an indirect dissociation (predissociation) pathway, where the system is directly excited to a bound (π, π*) state that undergoes a curve crossing (facilitated by spin-orbit coupling) to a repulsive (n, σ*) state. Later studies also identified an additional, direct dissociation pathway via a repulsive (n, σ*) state[4–6]. The branching ratio between the direct and indirect pathways is determined by the excitation energy and the nature of the substituents.

In monosubstituted benzenes, the effects of the different substituent halogen atoms manifest themselves in both mechanism and timescale. When excited at 266 nm, chlorobenzene features an indirect dissociation with a lifetime of ~1 ns[7], while bromobenzene undergoes indirect dissociation in 26 ps[7,8]. In iodobenzene, the indirect dissociation pathway with a decay-time of ~600 fs is complemented by a direct dissociation on a faster, ~400 fs[6,7] time scale. In mono-halogenated benzenes, the substitution of heavier halogens apparently accelerates curve crossing, presumably via stronger spin-orbit coupling of the initially excited (π, π*) state to the (n, σ*) repulsive surface[7,8]. In addition, the appearance of a second reaction pathway in iodobenzene likely indicates a shift in the relative energies of the excited states, which brings the direct pathway into play.

Para-disubstituted benzenes have been found to demonstrate similar trends. Excitation of p-dichlorobenzene at ~266 nm results in only the predissociation pathway, with dissociation occurring in 122 ps[9,10]. The situation is similar in p-dibromobenzene, but with a faster decay of 18.2 ps[11]. Initial photofragment translational energy studies of p-diiodobenzene suggested that predissociation occurs on a timescale faster than the rotational period of the molecule[1], and a recent ultrafast photoelectron study[12] suggests that the dissociation proceeds via curve crossing

from an initially excited bound state. However, no ultrafast studies of the wavepacket motion along the dissociative surface have been reported.

Ultrafast spectroscopy has long been used to study dissociation reactions[13,14], and photoelectron spectroscopy involving Rydberg states has more recently been shown to be an effective measure of structural dynamics[15–18]. The present investigation probes the photodissociation dynamics of p-diiodobenzene using time-resolved pump-probe photoelectron spectroscopy (see Figure 1). Following excitation at 271 nm, the dynamics of p-diiodobenzene is probed by multiphoton ionization via molecular Rydberg states using 405 nm photons. The photon energy matches the electronic transition energies between the dissociative states and the Rydberg resonances only at specific time delays. Consequently, measuring the travel times at which resonant ionization occurs can monitor the dissociation pathway.

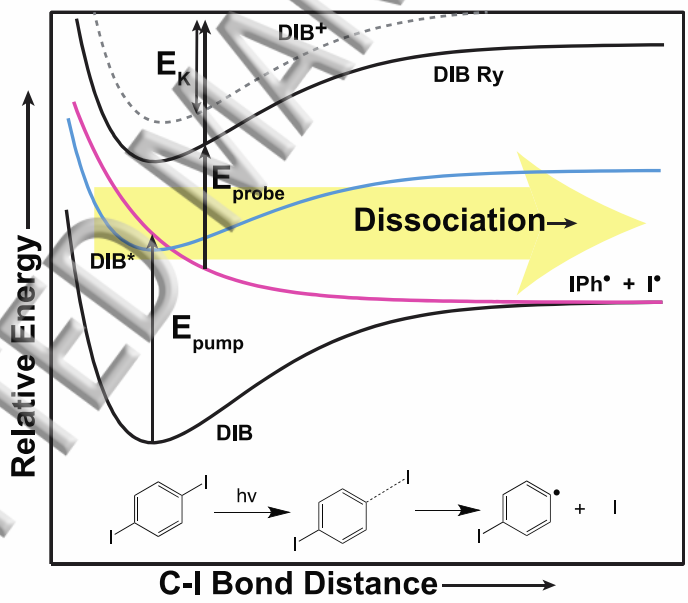

Figure 1. *Illustration of the experimental scheme and possible dissociation pathways of p-diiodobenzene (DIB) to the iodophenyl radical (IPh) and atomic iodine. The molecule is prepared in an excited state, DIB*, by the pump laser with photon energy* E_{pump}*. The time-delayed probe pulse with photon energy* E_{probe} *resonantly ionizes the dissociating molecule via Rydberg states, DIB Ry. The dissociation involves multiple electronic surfaces (not included in the illustration), which are revealed by their time-dependent resonant ionizations.*

METHODS

Photoelectron Spectroscopy

The experimental apparatus has been described in detail elsewhere[16,19,20]. A Ti:Sapphire regenerative amplifier (Coherent, Legend Elite Duo) generates approximately 35 fs pulses with a repetition rate of 5 kHz. The output beam is split, with 90% seeding an OPA (Coherent, OPerA Solo) that generates the pump pulse (4.58 eV, 0.05 eV FWHM, 2.4 μJ pulse energy), and 10% upconverted to the second harmonic using a BBO crystal as the probe pulse (3.06 eV, 0.04 eV FWHM, 8.0 μJ pulse energy). Both beams are focused perpendicularly onto a molecular beam created by heating solid 1,4-diiodobenzene to 140ºC to generate ~14 Torr of vapor, which is seeded in 1.1 bar of He gas. The ejected photoelectrons and ions are detected in a time-of-flight scheme by a microchannel plate detector with ultrafast timing electronics. The instrument function was determined via a Gaussian fit to the temporal response of acetone. The cross-correlation time between the pump and probe pulses was determined to be 98 ± 3 fs (FWHM).

UV-Visible Absorption Spectrometry

A Shimadzu UV-1700 double-beam scanning spectrometer (20 W, halogen lamp) was used to obtain the UV-visible absorption spectrum of 1,4-diiodobenzene from 190 nm to 400 nm. A small amount of solid sample was placed in the bottom of a sealed quartz cuvette with a path length of 1 cm, and the pressure was allowed to equilibrate before measurement of the vapor.

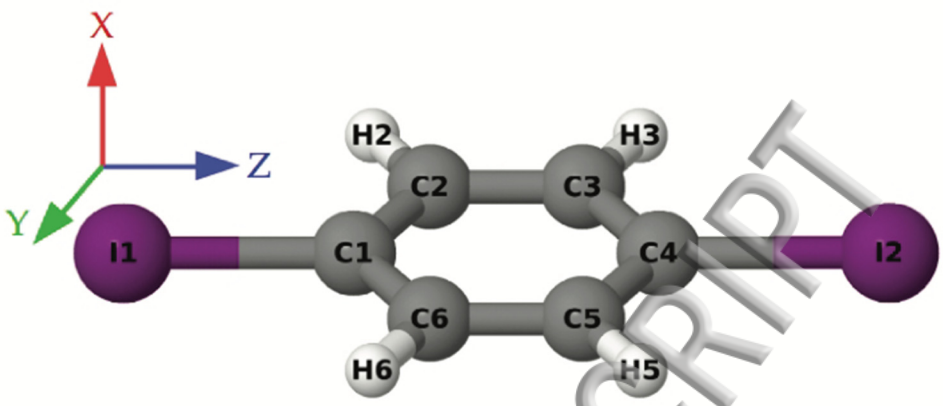

Figure 2. *Molecular structure of DIB, with Cartesian axes labeled in accordance to Table 2.*

All calculations described here are performed using the Molpro *ab initio* electronic structure program[21,22] and employ a correlation-consistent Dunning basis set of triple-zeta plus polarization quality (cc-pVTZ) for carbon and hydrogen atoms[23]. Iodine atoms are described by an effective core potential (ECP) for a 46-electron core, i.e. large-core [Kr]5d^{10}, with the larger cc-pVTZ-PP basis set of Peterson *et al*.[24] to describe the seven valence electrons. The ECP for iodine contains terms for the evaluation of spin-orbit coupling for the valence electrons.

The geometry of the 1^1A_1 ground state of DIB is optimized at the Complete Active Space Self-Consistent Field (CASSCF) level using a fourteen electrons in twelve orbitals active space, i.e. CASSCF(14,12), comprising the six benzene-like π orbitals and electrons and, for each iodine, the two C-I σ bond orbitals and electrons and the iodine p_x (out-of-plane, see Figure 2) lone pair of electrons. The 1^1A_1 ground state of DIB at the CASSCF(14,12) optimized geometry has a total energy of -251.777506 Hartree and a C-I bond length of 2.102 Å.

Following the work by Ajitha *et al*. on iodobenzene[25], the ground and the excited electronic states of DIB during photodissociation are studied by scanning the C-I bond distance of one C-I bond from 1.10 Å to 5.10 Å with the positions of the remaining atoms frozen, the symmetry of the molecule restrained to the C_{2v} point group, and the molecule located in the yz-

This manuscript was accepted by J. Chem. Phys. Click here to see the version of record.

plane (see Figure 2). The calculations are performed at the CASSCF(18,14) level with an active space that comprises all orbitals and electrons from the (14,12) space plus the iodine p_y (in-plane) lone pair for each iodine atom. Due to an orbital rotation between two orbitals in the B_2 irreducible representation (IR), specifically the C-C σ core orbital and the iodine p_y (in-plane) lone pair orbital, during unconstrained CASSCF optimization of the (18,14) active space orbitals, the core orbitals are frozen following an initial CASSCF(14,12) calculation. This places the iodine p_y orbitals correctly in the larger active space. The state-averaged (SA) CASSCF(18,14) calculation yields two roots in each IR of C_{2v} symmetry (A_1, B_1, B_2, A_2) of both singlet and triplet spin multiplicity. Calculations on the DIB^+ cation employ an analogous (17,14) active space using SA(8)-CASSCF, yielding two roots with doublet spin multiplicity in each IR.

To better account for the effect of dynamical electron correlation, Complete Active Space with Second Order Perturbation Theory (CASPT2) corrections are calculated using the SA(16)-CASSCF(18,14) wave function as reference. In this implementation the doubly external configurations are internally contracted, as are subspaces of the singly external and internal configuration spaces[26]. An imaginary level shift of 0.3 Hartree is employed to avoid intruder state problems and the carbon 1s orbitals are frozen in the CASPT2 calculations.

The spin-orbit coupling matrix elements in the basis of the 32 state-averaged CASSCF(18,14) states (8 singlets and 3x8 triplets) are evaluated from the ECP of iodine along the entire range of C-I distances using an ECP-only spin-orbit Hamiltonian as implemented in Molpro[21,22]. These are then combined with the diagonal elements of the spin-orbit free (SOF) adiabatic CASPT2 energies, giving rise to a treatment that accounts for both spin-orbit coupling and dynamical correlation[5]. The resulting matrix is diagonalized, producing a new set of adiabatic spin-orbit coupled (SOC) states, with 8 states in each IR derived from two singlet and six triplet states. In addition, the eigenvectors of the transformation to the SOC basis are used to derive SOC transition dipole moments (TDMs) from the corresponding SOF TDMs.

In principle, the ground state geometry of the molecule could be affected by the improved treatment of dynamical electron correlation in CASPT2. At the CASPT2 level, the optimized C-I bond length is R_{CI} = 2.072 Å, as determined by a numerical fit to the CASPT2 ground state potential energy curve, which is slightly shorter than the CASSCF(14,12) optimized value of 2.102 Å. This finding is in line with similar observations for the 1^1A_1 ground state in iodobenzene, where Sage *et al.*[5] found that MP2 predicted C-I bond lengths of 2.062 Å were somewhat shorter than the 2.120 Å predicted by CASSCF(12,10). Although the inclusion of spin-orbit coupling markedly changes the overall potential energy landscape, the position of the minimum of the SOC CASPT2 ground state is barely affected. The vertical transition properties listed in Table 1 are calculated at the CASSCF(14,12) optimized geometry, but with the two C-I bonds having the optimum CASPT2 bond length of 2.072 Å.

RESULTS

Ultrafast time-resolved photoelectron spectroscopy

The time-resolved, pump-probe photoelectron spectrum of DIB excited at 271 nm and probed with 405 nm photons is displayed in Figure 3. The spectral coordinate is the binding energy, which is the difference between the ionizing photon energy (3.06 eV) and the measured kinetic energy of the ejected electrons.

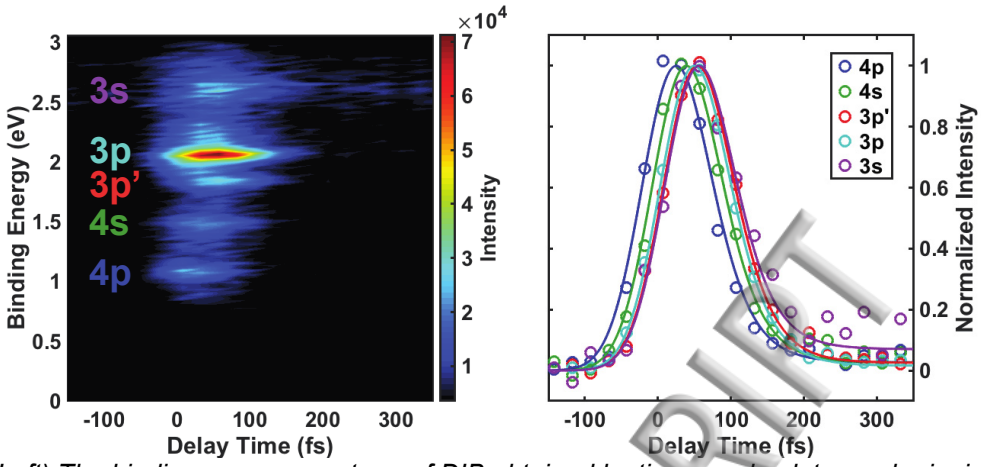

Figure 3. *(Left) The binding energy spectrum of DIB obtained by time-resolved, two-color ionization using 271 nm pump and 405 nm probe pulses. The intensity of the signal is given by the color as indicated by the color bar. (Right) Best fits of the time dependent transients using the model described in the text.*

The vertical ionization energy of DIB is 8.60 eV[27]. With an experimental pump energy of 271 nm (4.58 eV), a single 405 nm (3.06 eV) probe photon does not carry sufficient energy to ionize the molecule. Therefore, a two-photon ionization process is necessary to ionize out of the excited state with 405 nm photons (see Figure 1). This two-photon ionization is facilitated by intermediate Rydberg resonances, which are accessed at different pump-probe delay times as the molecule dissociates.

The spectrum shows five distinct photoelectron peaks, with binding energies of 1.07, 1.49, 1.85, 2.05, and 2.65 eV. These peaks can be assigned to Rydberg states with low principal quantum numbers based on the measured binding energy of each resonance. The quantum defect of a molecular Rydberg state is approximately given by

$$E_B = \frac{Ry}{(n-\delta)^2}, \qquad (1)$$

where E_B is the binding energy, Ry is the Rydberg constant (13.6 eV), n is the principal quantum number, and δ is the quantum defect. Given that typical quantum defect values are ~0.1 for nd Rydberg states, ~0.3-0.5 for np, and ~0.8-1 for ns states[28], the observed resonances can be assigned based on their experimentally measured quantum defects. It should be noted that these values are typical for second row elements. In the following assignments, we consider

This manuscript was accepted by J. Chem. Phys. Click here to see the version of record.

excitation from the HOMO, which belongs primarily to the pi system of the aromatic carbon ring, and thus we refer to the aforementioned values. This ignores possible excitation of the iodine lone pair, from which we would access Rydberg states with n ≥ 6.

The E_B = 1.07 eV resonance has (n - δ) = 3.56, implying a principal quantum number of 4 with a quantum defect of 0.43. This suggests that it is a 4p resonance. The next resonance, with E_B = 1.49 eV and consequently (n - δ) = 3.02, is assigned to 4s with δ = 0.98. The resonances at 1.85 and 2.05 eV both can be 3p states, with quantum defects of 0.29 and 0.42, respectively, and are thus labeled 3p and 3p'. The highest binding energy resonance, E_B = 2.65 eV, is identified as the 3s state with n=3 and δ = 0.73.

A visual inspection of the time dependent binding energy spectrum contour plot and the fits to the transients (Figure 3) shows that, in general, lower binding energy peaks are observed earlier than higher binding energy peaks. Evidently, different Rydberg resonances are accessed at different times during the dissociation process. To fit the time dependence of the Rydberg resonances we invoke a dynamical model adapted from the one developed for analyzing the ultrafast ring-opening reaction of 1,3-cyclohexadiene[16]. The model assumes that optical excitation leads initially to a state that is not involved in the dissociation of the bond. This model was found to be a better fit to the present experimental data than an alternate model that we have tested and that assumes direct excitation to a dissociative surface. The model used here is also in agreement with a previous study[12] that suggests that DIB is initially excited to a bound electronic state.

Following excitation, the DIB molecule undergoes a rapid curve crossing to the repulsive electronic state(s) with a time constant τ. The resulting wavepacket travels down the repulsive surface but can be ionized in a two-photon transition when the photon energy matches the energy difference between the repulsive surface and the bound Rydberg state.

This manuscript was accepted by J. Chem. Phys. Click here to see the version of record.

For a Rydberg state accessed directly from the initially excited bound state, the time evolution of the transient is given as,

$$I_{Ry}(t) = \int_0^t dt' e^{\frac{-t'}{\tau}}, \quad (2)$$

where τ represents the lifetime of the initially excited bound state, i.e. the decay time from the bound state(s) onto the repulsive surface(s). For those Rydberg states that are reached by resonant excitation from the dissociating surface, we assume that the wavepacket is launched on the dissociative surface as the molecule undergoes the electronic curve crossing with time constant τ, and travels down the repulsive surface for a time Δt before reaching the region where resonant excitation to the Rydberg state is energetically possible. The time dependence of the Rydberg signals therefore is

$$I_{Ry}(t) = \int_0^t dt' e^{\frac{-t'}{\tau}} e^{\frac{-(t-t'-\Delta t)^2}{2\sigma^2}}. \quad (3)$$

To adequately describe the experimental signals, $I_{Ry}(t)$ is then combined with a baseline that grows in at t=0 (arising from nonresonant ionization of the dissociating molecule), and convoluted with a Gaussian instrument function σ_{IF},

$$I(t) = \int_0^t dt' \left[c_1 I_{Ry}(t) + c_2 \delta_{0\ if\ t<0}^{1\ if\ t\geq 0}\right] e^{\frac{-(t-t')^2}{2\sigma_{IF}^2}}. \quad (4)$$

In the experiment, the resonance windows were found to be shorter than the temporal resolution and are therefore represented as Gaussian functions with a nominal width of σ = 1 fs. It is important to keep in mind that both Equation 2 and Equation 3 pertain to the indirect dissociation whereby the molecule is initially excited into a bound state.

The parameters of the best fits to this model are listed in Table 1. We find that the time dependence of the 4p Rydberg transient is best described by Equation 2, implying that it arises from the ionization out of the initially excited bound state. All other resonances are best modeled by Equation 3, suggesting that they stem from the process where the wavepacket decays from the initially excited state and travels down the dissociative surface(s). The ballistic trajectories of

the wavepackets are represented by the increasing traveling times Δt observed for resonances with progressively higher binding energies. All transients can be fit to the same lifetime of the bound state, τ = 33 ± 4 fs. This value is in excellent agreement with the previously reported lifetime of the initially excited state of 35 ± 10 fs[12].

			Dynamic Fit	
Quantum Defect	**Peak Assignment**	**Binding Energy (eV)**	**τ (fs)**	**Δt (fs)**
N/A	B_1	3.94	35 ± 10	N/A
0.43	4p	1.07		N/A
0.98	4s	1.49		14 ± 5
0.29	3p'	1.85	33 ± 4	29 ± 4
0.42	3p	2.05		24 ± 4
0.73	3s	2.65		31 ± 5

Table 1. *Fit parameters of the dynamical model applied to the binding energy transients in the two-color photoionization spectrum of DIB. All errors are reported to 3 sigma. The list includes the B_1 valence state data that has been previously reported[12], and which was recorded using one-photon ionization with 300 nm probe photons. All other entries are from the experiments reported here and are with two-photon ionization using 405 nm probe photons. The B_1 data was fit independently of the Rydberg progression observed in the present two-photon ionization experiment.*

Calculations

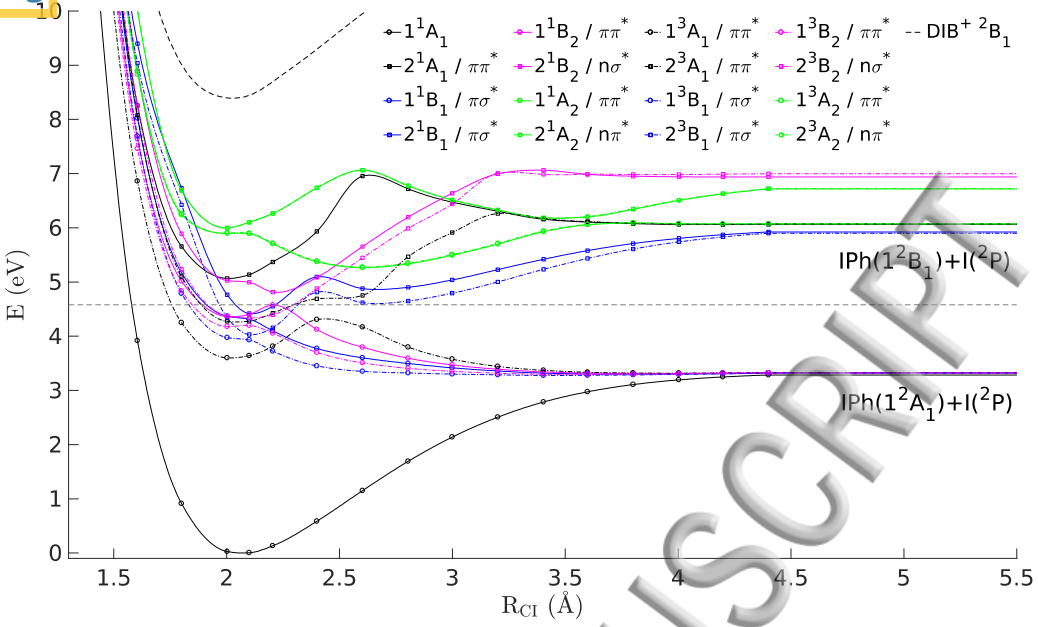

***Figure 4A**. Adiabatic CASPT2(18,14) spin-orbit free potential energy curves (PECs) along one of the two C-I bonds in neutral DIB, and the corresponding CASPT2(17,14) PEC for the DIB⁺ cation ground state. State labels include the dominant character for the vertical excitation from the 1^1A_1 DIB ground state, and the asymptotic dissociation limits are as labeled. The horizontal dashed line represents the pump laser photon energy.*

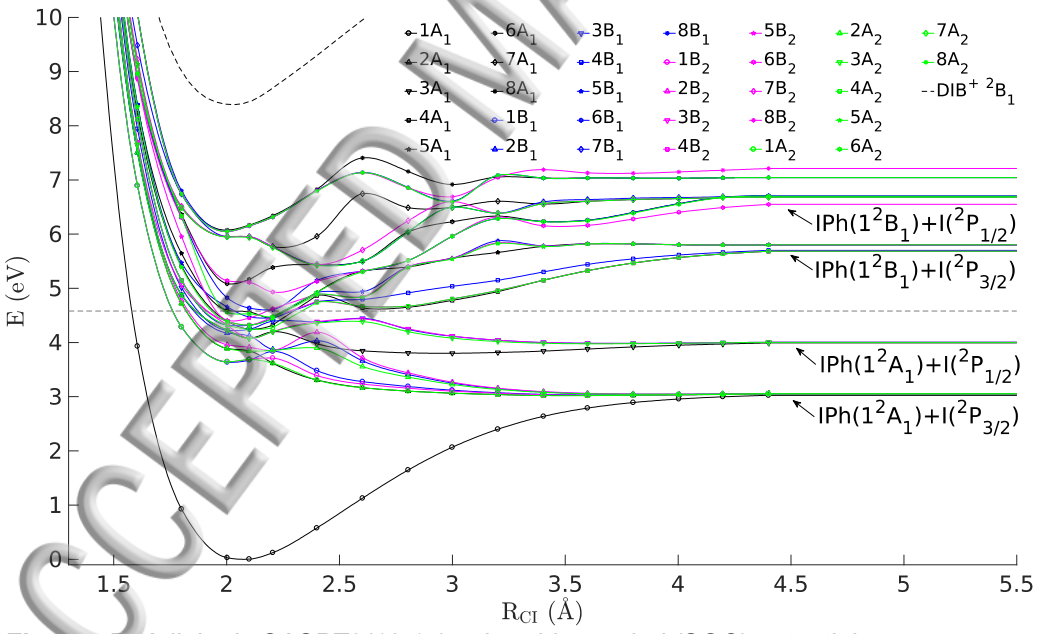

***Figure 4B**. Adiabatic CASPT2(18,14) spin-orbit coupled (SOC) potential energy curves (PECs) along one of the two C-I bonds in neutral DIB, and the corresponding CASPT2(17,14) PEC for the DIB⁺ cation ground state. The spin-orbit coupling is inferred from CASSCF(18,14) calculations. The strictly adiabatic SOC states result from mixing of the spin-orbit free (SOF) states and obey the non-crossing rule in each IR. Hence, their adiabatic SOF composition does not vary smoothly. The horizontal dashed line represents the pump laser photon energy.*

State	Electronic Transition	CASPT2 Weights of SOF states	TDM (D)	$E_{vertical}$ (eV)
$1A_1$	--	98.8% 1^1A_1	--	0.00
$1B_1$	(π,π*)	98.7% 1^3A_1	0.121 (x)	3.68
$1A_2$	(π,π*)	98.2% 1^3A_1, 1.0% 1^3B_1	0	3.68
$1B_2$	(π,π*)	99.4% 1^3A_1	0.030 (y)	3.69
$2A_2$	(π,σ*)/(n,σ*)	76.9% 1^3B_1, 20.2% 2^3B_2, 1.6% 1^3A_1, 1.1% 2^3B_1	0	3.84
$2A_1$	(π,σ*)/(n,σ*)	75.8% 1^3B_1, 22.0% 2^3B_2, 2.0% 2^3B_1	0.141 (z)	3.84
$2B_2$	(π,σ*)	93.3% 1^3B_1, 5.5% 2^1B_2	0.209 (y)	3.92
$3A_2$	(π,σ*)	97.4% 2^3B_1, 2.2% 1^3B_1	0	4.07
$3B_2$	(π,σ*)	98.9% 2^3B_1	0.033 (y)	4.07
$3A_1$	(π,σ*)	97.1% 2^3B_1, 2.3% 1^3B_1	0.015 (z)	4.09
$2B_1$	(π,σ*)/(n,σ*)	48.7% 1^1B_1, 47.9% 2^3B_2, 2.0% 2^1B_1	0.476 (x)	4.12
$3B_1$	(π,π*)	99.6% 1^3B_2	0.006 (z)	4.25
$4A_1$	(π,π*)	99.6% 1^3B_2	0	4.25
$4A_2$	(π,π*)	99.0% 1^3B_2	0.013 (x)	4.25
$4B_1$	(π,π*)	97.0% 2^3A_1, 2.4% 2^1B_1	0.110 (x)	4.32
$5A_2$	(π,π*)	99.8% 2^3A_1	0	4.32
$4B_2$	(π,π*)	99.9% 2^3A_1	0.006 (y)	4.32
$5B_2$	(π,π*)	99.9% 1^1B_2	0.286 (y)	4.45
$5B_1$	**(π,σ*)**	**84.6% 2^1B_1, 10.7% 1^1B_1, 2.1% 2^3B_2, 2.1% 2^3A_1**	**0.520 (x)**	**4.46**
$6A_2$	(n,σ*)	78.7% 2^3B_2, 19.8% 1^3B_1, 1.2% 2^3B_1	0	4.53
$5A_1$	(n,σ*)/(π,σ*)	77.4% 2^3B_2, 21.4% 1^3B_1	0.162 (z)	4.56
$6B_1$	**(n,σ*)/(π,σ*)**	**48.8% 2^3B_2, 39.8% 1^1B_1, 10.1% 2^1B_1**	**0.574 (x)**	**4.65**
$6B_2$	(n,π*)	94.2% 2^1B_2, 5.4% 1^3B_1	0.847 (y)	5.11
$6A_1$	(π,π*)	98.3% 2^1A_1, 1.7% 2^3A_2	5.972 (z)	5.17
$7A_2$	(π,π*)	100.0% 1^1A_2	0	5.94
$7A_1$	(π,π*)	99.9% 1^3A_2	0.013 (x)	5.95
$7B_1$	(π,π*)	99.9% 1^3A_2	0.130 (z)	5.95
$7B_2$	(π,π*)	99.9% 1^3A_2	0.007 (y)	5.95
$8B_2$	(n,π*)	99.9% 2^3A_2	0.019 (y)	6.15
$8B_1$	(n,π*)	99.8% 2^3A_2	0.021 (x)	6.15
$8A_2$	(n,π*)	99.9% 2^1A_2	0	6.16
$8A_1$	(n,π*)	98.3% 2^3A_2, 1.7% 2^1A_1	0.812 (z)	6.17
DIB^+	1^2B_1	Ground-state		8.41

***Table** 2. Electronic state labels, the main character of the dominant spin-orbit free (SOF) component of each electronic transition (with two characters provided if the second largest SOF component has a weight >20%), percentage weights of the dominant SOF components of each spin-orbit coupled (SOC) state at equilibrium geometry (only states with contributions larger than 1% are included), total transition dipole moments (TDM) in Debye (with the main axis identified in accordance to Fig. 2), and vertical excitation energies in eV. The data provided pertains to the SA(32)-CASPT2(18,14) SOC potential energy curves, with the vertical ionization energy taken from the SOF CASPT2(17,14) ground state energy of the DIB^+ cation. Energies are evaluated at the CASPT2 optimized geometry, with a C-I bond length of 2.072 Å.*

This manuscript was accepted by J. Chem. Phys. Click here to see the version of record.

The calculated adiabatic CASPT2(18,14) potential energy curves (PECs) along the C-I bond distance are shown in Figure 4. Figure 4A shows the spin-orbit free (SOF) adiabatic states, while Figure 4B shows the spin-orbit coupled (SOC) states. The calculations retain C_{2v} symmetry throughout, preserving planarity and assuming that the dissociation proceeds along the z-axis. The non-adiabatic coupling between excited states of different symmetries is zero. This allows the dissociation dynamics to be viewed as four independent processes occurring in each of the four groups of states (A_1, B_1, B_2, A_2), where the initial conditions are set by the selection rules and the probability of a vertical excitation in the Franck-Condon (FC) region to each individual state.

The reduction of the multidimensional potential energy surfaces (PESs) to the single dissociation coordinate given by the PECs effectively means that the non-adiabatic population transfers are treated as occurring at pseudo avoided-crossings instead of true conical intersections. It should be noted that the SOC PECs are highly mixed and the composition given in Table 2 is only valid at the CASPT2/cc-pVTZ-PP optimized ground state geometry; at other geometries the composition changes. The states are coupled by non-adiabatic coupling, which is known to be fairly localized and which manifests itself in sharply peaked non-adiabatic coupling matrix elements (NACMEs) at the pseudo avoided-crossings. The singlet and triplet manifolds are further connected by spin-orbit coupling, which is less localized, varies slowly and shows an asymptotic behavior at infinite $R_{C\text{-}I}$ that correlates with the coupling in atomic iodine. At large internuclear separation, seven excited states and the ground state (two of each symmetry in total) correlate with the $I(^3P_{3/2})$ + IPh(X, $^2A_1$) asymptotic limit, whereas four states (one of each IR) correlate with the $I(^3P_{1/2})$ + IPh(X, $^2A_1$) limit.

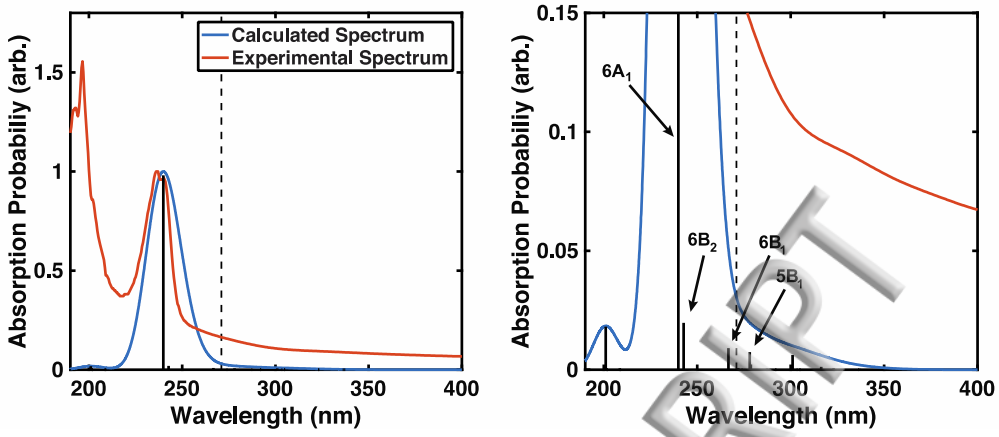

Figure 5. *Experimentally measured UV absorption spectrum of DIB, together with the calculated spectrum according to data in Table 2. The left panel gives the overall spectrum, while the right panel shows the region close to the excitation energy used in the current time-resolved experiment (vertical dashed lines in both panels).*

Taking into account the oscillator strengths and vertical excitation energies in Table 2, there appears to be a reasonable correspondence between the theoretical spectrum and the experimentally measured optical absorption spectrum, see Figure 5. For this figure, the calculated vertical transitions from Table 2 are scaled by the square of the transition dipole moment and convoluted with a spectral width of σ = 0.2 eV. The experimental absorption spectrum is scaled to match the most intense peak near 240 nm. The absorption spectrum is dominated by the transition to the $6A_1$ state at ~240 nm, which has an oscillator strength an order of magnitude greater than all other states in this energy region. Note that the experimental spectrum has a peak at ~200 nm that is even more intense than the 240 nm peak. In our calculations, there is a reasonably intense peak at ~201 nm due to $8A_1$. It could be that our calculations, which do not account for the effect of nuclear motion on the absorption spectrum, underestimate the intensity of that absorption, or that there is a nearby state at that energy that is not included in our calculations, since $8A_1$ is the highest energy state in our calculations. Based on the good agreement between the calculated and the observed absorption spectra of DIB, we conclude that the accuracy of the predicted vertical excitation energies and transition dipole moments is reasonable.

This manuscript was accepted by J. Chem. Phys. Click here to see the version of record.

From Table 2 it follows that at the 4.58 eV excitation energy of our experiments, and allowing for a ±0.1 eV uncertainty in the calculated excitation energies, there are 21 energetically accessible excited states. Out of those, the calculated oscillator strengths (not shown in the table) for a vertical transition above the ground $1A_1$ state suggest that a significant initial population can be excited onto the $2B_1$ ($f=35.3\times10^{-4}$), $5B_2$ ($f=13.8\times10^{-4}$), $5B_1$ ($f=45.8\times10^{-4}$), and $6B_1$ ($f=58.1\times10^{-4}$) states. The strength of the transitions to these states can be traced to the large contribution of the singlet SOF 1^1B_1, 2^1B_1, and 2^1B_2 states to the SOC states in the Franck-Condon (FC) region, with transition dipole moments of 0.484(x), 0.792(x), and 0.892(y) Debye (see Supplementary Material). Although the $6B_2$, $6A_1$ and $8A_1$ states have much greater oscillator strengths, they lie significantly above the experimental excitation energy and are considered inaccessible in the current experiment. Also note that the SOC states that belong to the A_2 group cannot be accessed by excitation from the ground state, which belongs to the A_1 IR, as seen from the corresponding TDM integral selection rules, making the A_2 manifold optically dark. In addition, SOC states that have a significant contribution from the SOF A_2 states in the FC region have vanishingly small TDMs on account of the selection rules in the SOF picture.

Finally, taking into account the pump pulse energy and the magnitude of the TDMs, we conclude that the initial absorption most likely excites the $5B_1$ and $6B_1$ states. This assignment agrees with a previous study[12], which suggested that the initially excited state is a bound electronic state. Although the pump pulse bandwidth (0.05 eV) is less than the calculated energy difference between the $5B_1$ and $6B_1$ states in the Franck-Condon region ($\Delta E=0.19$ eV), these bound states support vibrational levels and are thus expected to have a Franck-Condon envelope larger than the laser bandwidth. Absorption into the $5B_2$ state is also possible, but this is dismissed here due to the comparatively small transition strength compared to the B_1 states.

In the adiabatic picture, the energy difference between the initially populated $5B_1$ and $6B_1$ states and the dissociative states $1B_1$, $2B_1$ and $3B_1$ states indicates that dissociation

This manuscript was accepted by J. Chem. Phys. Click here to see the version of record.

proceeds via a cascade of non-adiabatic transitions leading to one of the repulsive states. However, a physically more intuitive picture is encoded in the 1-8B_1^s semi-diabatic states shown in Figure 6. These states are defined such that their SOF composition varies smoothly. Computationally this is realized by maximizing the overlap between the eigenvectors of the SOF to SOC transformation between successive points on the curves. The semi-diabatic states are admixtures of SOF states, whose contribution varies along the carbon-iodine bond distance, R_{CI}. In instances where the spin-orbit coupling is weak, these states can significantly resemble or even match the SOF states from which they originate. However, the semi-diabatic curves are not character-preserving, i.e. they formally behave like the SOF adiabatic curves exhibiting pseudo-avoided crossings. A mathematically rigorous formulation of the corresponding diabatic states is in principle possible via a transformation of the non-adiabatic coupling matrix elements (NACMEs) to the SOC basis[29]. Presently, the diabatic SOC $5B_1^d$ and $6B_1^d$, which follow the character of the $5B_1^s$ and $6B_1^s$ in the FC region, are formed by inspection of the *ab initio* configuration interaction coefficients, and are presented in Figure 6. These diabatic states give an intuitive view of the dissociation pathway.

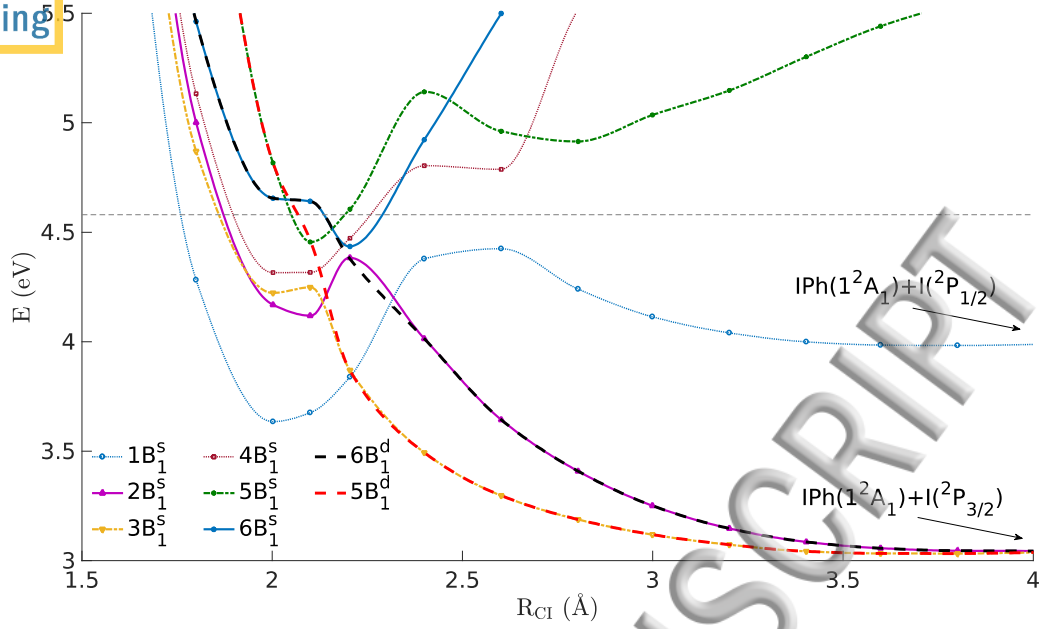

***Figure 6**. Semi-diabatic spin-orbit coupled (SOC) states belonging to the B_1 symmetry, labelled 1-8B_1^s. The spin-orbit free composition of these states varies smoothly, and the curves can cross. The fully diabatic (character-preserving) paths following excitation to the 5B_1^s and 6B_1^s adiabatic SOC states are given as dashed lines and are labelled 5B_1^d and 6B_1^d respectively.*

As a general remark, it must be recognized that the reduction of dimensionality inherent in the *ab initio* calculations results in an oversimplified picture of the dynamics, as if happening exclusively on a single family of states. A more accurate, but computationally prohibitive (the current calculations require in excess of 436 CPU hours per point on a single processor), treatment would account for the coupling between states belonging to different IR in the C_{2v} point group in the symmetry-breaking direction at the vicinity of avoided-crossings. In addition, our treatment does not account for the geometry relaxation of the iodophenyl fragment. The complete removal of the iodine atom bonded to C4 shortens the remaining C1-I bond from 2.102 Å to 2.070 Å at the CASSCF(14,12) level of theory, and is also associated with ring relaxation. The latter manifests itself in shortening of the C3-C4 and C4-C5, and elongation of C2-C3 and C5-C6 bonds compared to DIB. Comparable effects on the geometry should be expected at the CASPT2(18,14) level. Such structure relaxations associated with each point along the C-I dissociation coordinate are likely to affect the energies of the ground and the

This manuscript was accepted by J. Chem. Phys. Click here to see the version of record.

excited states as well as the position of the pseudo avoided-crossings. Ultimately, such effects could be explored using on-the-fly dynamics simulations[30–32]. However, for this to be feasible more efficient electronic structure calculations would be required. We also note that the constriction of the C-I bond, 0.032 Å, is smaller than the FWHM of the ground state v=0 wavefunction, which is about 0.09 Å.

DISCUSSION

Inspection of the quantum defects of the experimentally observed Rydberg resonances (Table 1) shows that the value for the 3p peak (0.42) is almost identical to that of the 4p peak (0.43). The different observation times of those peaks therefore implies that their quantum defects are not strongly affected by the dissociation of the C-I bond. It is likely, then, that these Rydberg orbitals have nodes along the C-I axis, making them less sensitive to structure changes along the dissociation coordinate[33,34]. This suggests that they could be either p_x or p_y orbitals. It is furthermore important to note that the probe pulses are polarized perpendicularly relative to the pump pulse. The computational results show that the initial excitation has a transition dipole moment oriented perpendicular to the plane of the molecule (x direction, see Figure 2), and so the out-of-plane p_x orbital is preferentially probed at short delay times, before the molecule has time to rotate (assuming C_{2v} symmetry). Combining the two arguments, we conclude that the 1.07 eV and 1.85 resonances can be identified as the $4p_x$ and $3p_x$ resonances, respectively. The 3p' peak has a quantum defect that is significantly different from the 3p and 4p resonances. There are several possible explanations for this observation, which will be discussed below.

The resonance observed with the longest time delay, the 3s peak, has a quantum defect that differs notably from that of the 4s peak (0.73 vs. 0.98). This is consistent with the fact that ns Rydberg states have significant electron density in the region of the dissociating C-I bond, so that the quantum defect is expected to change as the molecular structure evolves.

We find that most travel times Δt listed in Table 1 increase monotonically with the binding energies of the Rydberg resonances. This is rational since Rydberg states with larger binding energies are lower in total energy, and therefore come later into resonance with the energy of the dissociative state given the fixed probe photon energy. It is then interesting to observe that the 3p' peak with a binding energy of 1.85 eV is seen *after* the 3p peak with a binding energy of 2.05 eV. The most natural explanation is that the 3p' transient arises from ionization out of a different dissociative surface, as illustrated in Figure 7. The temporal sequence of the binding energy transients therefore indicates that the 3p' resonance arises from a higher energy dissociative valence state than the 4s, 3p, and 3s resonances. This is in excellent agreement with the CASPT2 calculations, which show that the initial excitation may lead to either of two close-lying B_1 states. Specifically, the initial excitation most likely populates both the $5B_1$ and $6B_1$ states. Those states eventually couple to the dissociative $3B_1$ and $2B_1$ states, respectively. Thus, it is possible that the 3p' resonance arises from the dissociation on the $2B_1$ state accessed via the $6B_1$ state, while the 4s, 3p, and 3s resonances show the dissociation on $3B_1$ state, which is accessed from excitation to the $5B_1$ state (see Figure 7).

The observation of a series of resonances from the $3B_1$ state, in contrast to only the single 3p' resonance from the $2B_1$ state, could reflect either the relative populations of the two surfaces in the optical excitation or differences in the valence-to-Rydberg-state excitation cross-sections for the two states. Given the smaller observed intensity of the 3p' resonance compared to the 3p resonance, it is likely that other Rydberg transitions from the $2B_1$ state are of too low intensity to be observed in the experiment. Note that any other Rydberg series due to spin-orbit coupling in the cation are not considered presently.

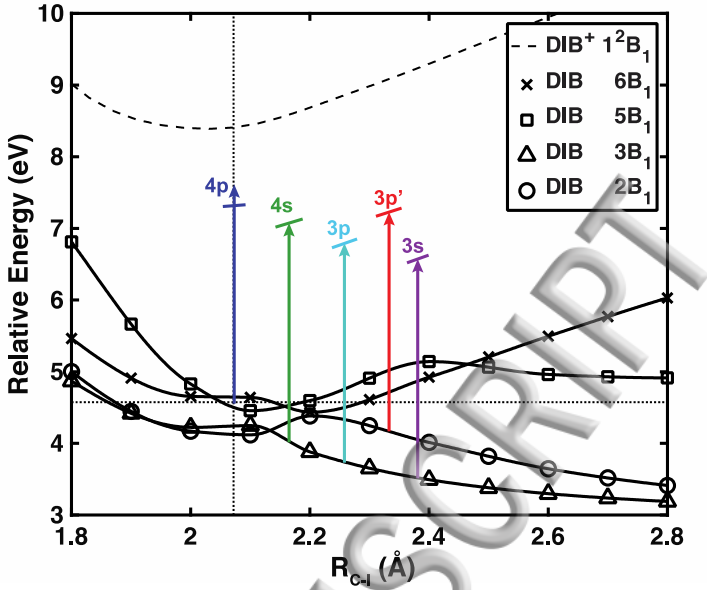

Figure 7. *The experimentally observed Rydberg resonances as a function of dissociating C-I distance (R_{C-I}), as determined by fitting to the relevant CASPT2 calculated potential energy curves. The experimental excitation energy is shown as a horizontal dashed line, and the CASPT2 optimized ground state C-I distance is shown as a vertical dashed line.*

Experiment			Theory		
Ry State	**Δt (fs)**	**BE + hν (eV)**	**Ion – Ex (eV)**	**ΔR (Å)**	**Ex State**
4p	0	4.13	3.83	2.07	$5B_1/6B_1$
4s	14	4.55	4.55	2.16	$3B_1$
3p'	29	4.91	4.91	2.33	$2B_1$
3p	24	5.11	5.11	2.26	$3B_1$
3s	31	5.71	5.71	2.38	$3B_1$

Table 3. *Fit results of the experimentally observed Rydberg resonances to the binding energies of the CASPT2 calculated potential energy curves.*

Based on the valence state assignments discussed above, we can combine the experimental results with the calculated potential energy curves to determine the C-I distance of the dissociating molecule as a function of time. For each Rydberg resonance, we fit the sum of the experimental binding energy and the probe photon energy to the calculated energy difference between the ion ground state and the assigned valence state (see Table 3), thus correlating the measured Δt with the dissociating C-I distance. The 4p resonance, arising from a superposition of bound states, was placed at the ground state equilibrium bond length of 2.072

This manuscript was accepted by J. Chem. Phys. Click here to see the version of record.

Å. For this state, the sum of the experimental binding energy and the probe photon energy is found to be 0.30 eV larger than the calculated energy difference between the ion ground state and the initial excitation energy. Given that the valence-Rydberg absorption occurs between two bound electronic surfaces, it is reasonable to attribute this to the deposition of vibrational energy in the Rydberg state, which is then preserved in the ionization step.

The fit of the experimentally measured travel time Δt to the dissociating C-I bond distance outlined in Table 3 allows us to track the wavepacket motion along the $3B_1$ surface. The measured travel time of 10 fs between the 4s and 3p resonances gives a wavepacket velocity of 0.010 Å/fs (Figure 8). Between the 3p and 3s resonances, the wavepacket velocity is 0.017 Å/fs, revealing the acceleration of the dissociating wavepacket caused by the repulsive surface.

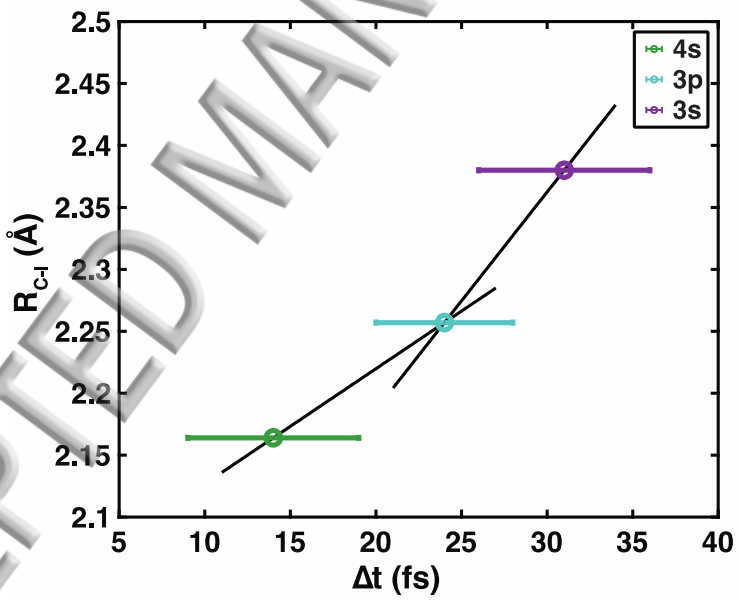

Figure 8. *The C-I bond distances of the dissociating molecule, R_{C-I}, vs. the travel time Δt, based on resonances accessed from the $3B_1$ valence state. The intersecting lines give wavepacket velocities of 0.010 Å/fs and 0.017 Å/fs, respectively. The error bars represent the 3σ uncertainty in the fit to the time dependence of the experimentally measured Rydberg resonances (also shown in Table 1).*

Finally, we note that the differing quantum defect of the 3p' peak as compared to the 3p and 4p resonances is not yet definitively explained. The two involved repulsive surfaces ($2B_1$ and $3B_1$) have the same symmetry, so that the selection rules for Rydberg transitions are the

This manuscript was accepted by J. Chem. Phys. Click here to see the version of record.

same in the C_{2v} picture. This means it is unlikely that the 3p' peak is a $3p_y$ or $3p_z$ orbital if the molecule retains C_{2v} symmetry. It is possible that, because the $2B_1$ state (from which the 3p' resonance is accessed) is of mixed singlet/triplet character, the 3p' resonance arises from a singlet Rydberg series, whereas the other resonances belong to a triplet series. Alternatively, it is possible that the avoided crossing from the $5B_1$ to $2B_1$ surface breaks the C_{2v} symmetry, so that transitions to the $3p_y$ and $3p_z$ resonances are allowed.

CONCLUSION

Upon excitation with a 4.58 eV laser pulse, 1,4-diiodobenzene is found to dissociate via an ultrafast indirect dissociation pathway. The initially excited $5B_1$ and $6B_1$ bound states decay into the repulsive $2B_1$ and $3B_1$ states with a 33 ± 4 fs time constant. As the molecule travels down the repulsive surfaces, the probe laser pulse comes into resonance with molecular Rydberg states in a sequential fashion. The assignment of the dissociative states based on CASPT2 calculations is tentative but in good agreement with the observed binding energy transients as well as with a previous study[12].

The observation of the fast indirect dissociation pathway as the dominant reaction mechanism is informative. The increase in spin-orbit coupling caused by the substitution by iodine as compared to lighter halogen atoms causes a significant increase in the rate of nonadiabatic internal conversion in p-diiodobenzene (33 fs) compared to p-dibromobenzene (18.2 ps[11]) and p-dichlorobenzene (122 ps[9,10]). In addition, the fact that direct dissociation is not observed indicates that the system exhibits qualitatively different behavior than the monosubstituted iodobenzene, which undergoes dissociation via both direct and indirect pathways[6,7]. The absence of an observed direct pathway could be the result of a shift in the energies of the repulsive surfaces relative to iodobenzene. The calculated semi-diabatic states $5B_1^s$ and $6B_1^s$ provide some indication of how these dissociations proceed through the network of adiabatic electronic states. In conclusion, diiodobenzene provides a stark reminder of the

complexity of even apparently simple dissociation dynamics in molecules with a high density of states and strong spin-orbit coupling.

SUPPLEMENTARY MATERIAL

See supplementary material for calculated SOF and SOC potential energy curves, as well as the optimized ground state geometry of DIB and a summary of the calculated SOF excitation transitions.

ACKNOWLEDGMENTS

This study was supported by the Army Research Office (grant # W911NF-17-1-0256). BMS acknowledges funding from the NASA Rhode Island Space Grant Consortium and a Brown University Vince Wernig fellowship. AK acknowledges funding from the Leverhulme Trust (RPG-2013-365) and a collaborative research grant from the Carnegie Trust. NZ acknowledges a Carnegie PhD Scholarship. Part of the computational work reported used the ARCHER UK National Supercomputing Service (http://www.archer.ac.uk) and the Edinburgh Compute and Data Facility (ECDF) (http://www.ecdf.ed.ac.uk).

REFERENCES

[1] M. Kawasaki, S.J. Lee, and R. Bersohn, J. Chem. Phys. **66**, 2647 (1977).

[2] M. Dzvonik, S. Yang, and R. Bersohn, J. Chem. Phys. **61**, 4408 (1974).

[3] A. Freedman, S.C. Yang, M. Kawasaki, and R. Bersohn, J. Chem. Phys. **72**, 1028 (1980).

[4] S. Unny, Y. Du, L. Zhu, K. Truhins, R.J. Gordon, A. Sugita, M. Kawasaki, Y. Matsumi, R. Delmdahl, D.H. Parker, and A. Berces, J. Phys. Chem. A **105**, 2270 (2001).

[5] A.G. Sage, T.A.A. Oliver, D. Murdock, M.B. Crow, G.A.D. Ritchie, J.N. Harvey, and M.N.R.

A. Asfold, Phys. Chem. Chem. Phys. **13**, 8075 (2011).

[6] P.Y. Cheng, D. Zhong, and A.H. Zewail, Chem. Phys. Lett. **237**, 399 (1995).

[7] M. Kadi, J. Davidsson, A.N. Tarnovsky, M. Rasmusson, and E. Åkesson, Chem. Phys. Lett. **350**, 93 (2001).

[8] X.-P. Zhang, Z.-R. Wei, Y. Tang, T.-J. Chao, B. Zhang, and K.-C. Lin, ChemPhysChem **9**, 1130 (2008).

[9] R.-S. Zhu, H. Zhang, G.-J. Wang, X.-B. Gu, K.-L. Han, G.-Z. He, and N.-Q. Lou, Chem. Phys. **248**, 285 (1999).

[10] L.-W. Yuan, J.-Y. Zhu, Y.-Q. Wang, L. Wang, J.-L. Bai, and G.-Z. He, Chem. Phys. Lett. **410**, 352 (2005).

[11] M. Kadi and J. Davidsson, Chem. Phys. Lett. **378**, 172 (2003).

[12] B. Stankus, J.M. Budarz, A. Kirrander, D. Rogers, J. Robinson, T.J. Lane, D. Ratner, J. Hastings, M.P. Minitti, and P.M. Weber, Faraday Discuss. **194**, 525 (2016).

[13] M.J. Rosker, M. Dantus, and A.H. Zewail, J. Chem. Phys. **89**, 6113 (1988).

[14] M. Dantus, M.J. Rosker, and A.H. Zewail, J. Chem. Phys. **89**, 6128 (1988).

[15] X. Cheng, Y. Zhang, Y. Gao, H. Jónsson, and P.M. Weber, J. Phys. Chem. A **119**, 2813 (2015).

[16] C.C. Pemberton, Y. Zhang, K. Saita, A. Kirrander, and P.M. Weber, J. Phys. Chem. A **119**, 8832 (2015).

[17] Y. Zhang, S. Deb, H. Jónsson, and P.M. Weber, J. Phys. Chem. Lett. **8**, 3740 (2017).

[18] Y. Zhang, H. Jónsson, and P.M. Weber, Phys. Chem. Chem. Phys. **19**, 26403 (2017).

[19] B. Kim, N. Thantu, and P.M. Weber, J. Chem. Phys. **97**, 5384 (1992).

[20] C.P. Schick, S.D. Carpenter, and P.M. Weber, J. Phys. Chem. A **103**, 10470 (1999).

[21] H.J. Werner, P.J. Knowles, G. Knizia, F.R. Manby, M. Schütz, P. Celani, T. Korona, R. Lindh, A. Mitrushenkov, G. Rauhut, and others, See Http//www. Molpro. Net (2012).

[22] H.J. Werner, P.J. Knowles, G. Knizia, F.R. Manby, and M. Schütz, Wiley Interdiscip. Rev. Comput. Mol. Sci. **2**, 242 (2012).

[23] T.H. Dunning Jr, J. Chem. Phys. **90**, 1007 (1989).

[24] N.B. Balabanov and K.A. Peterson, J. Chem. Phys. **125**, (2006).

[25] D. Ajitha, D.G. Fedorov, J.P. Finley, and K. Hirao, J. Chem. Phys. **117**, 7068 (2002).

[26] P. Celani and H.-J. Werner, J. Chem. Phys. **112**, 5546 (2000).

[27] A.W. Potts, M.L. Lyus, E.P.F. Lee, and G.H. Fattahallah, J. Chem. Soc. Faraday Trans. 2 Mol. Chem. Phys. **76**, 556 (1980).

[28] J.W. Rabalais, *Principles of Ultraviolet Photoelectron Spectroscopy* (John Wiley & Sons, 1977).

[29] G. Granucci, M. Persico, and G. Spighi, J. Chem. Phys. **137**, (2012).

[30] M.P. Minitti, J.M. Budarz, A. Kirrander, J.S. Robinson, D. Ratner, T.J. Lane, D. Zhu, J.M. Glownia, M. Kozina, H.T. Lemke, M. Sikorski, Y. Feng, S. Nelson, K. Saita, B. Stankus, T. Northey, J.B. Hastings, and P.M. Weber, Phys. Rev. Lett. **114**, 1 (2015).

[31] A. Kirrander, K. Saita, and D. V Shalashilin, J. Chem. Theory Comput. **12**, 957 (2016).

[32] D. Bellshaw, D.A. Horke, A.D. Smith, H.M. Watts, E. Jager, E. Springate, O. Alexander, C. Cacho, R.T. Chapman, A. Kirrander, and R.S. Minns, Chem. Phys. Lett. **683**, 383 (2017).

[33] X. Liang, M.G. Levy, S. Deb, J.D. Geiser, R.M. Stratt, and P.M. Weber, J. Mol. Struct. **978**, 250 (2010).

[34] J.L. Gosselin and P.M. Weber, J. Phys. Chem. A **109**, 4899 (2005).